Role of nanoparticle layer in determining minimum heat flux temperature during quenching of high-temperature body

UMEHARA, Yutaro
Department of Mechanical and Intelligent Systems Engineering, The University of Electro-Communications

OKAWA, Tomio
Department of Mechanical and Intelligent Systems Engineering, The University of Electro-Communications

出版情報：Mechanical Engineering Journal. 8 (4), pp.20-00527-, 2021. 日本機械学会
バージョン：

Bulletin of the JSME Vol.8, No.4, 2021
Mechanical Engineering Journal

Role of nanoparticle layer in determining minimum heat flux temperature during quenching of high-temperature body

Yutaro UMEHARA* and Tomio OKAWA*
*Department of Mechanical and Intelligent Systems Engineering, The University of Electro-Communications
1-5-1, Chofugaoka, Chofu-shi, Tokyo 182-8585, Japan
E-mail: umehara@eel.mi.uec.ac.jp

Received: 11 December 2020; Revised: 28 January 2021; Accepted: 2 March 2021

Abstract
Nanofluid, a liquid containing choroidal dispersion of nanometer-sized solid particles, enables high-temperature bodies to be cooled more rapidly during quenching than in pure liquid. Drastic rise of the minimum heat flux temperature (T_{MHF}) caused by the layer of nanoparticles formed on the heat transfer surface is the key phenomenon of heat transfer enhancement. In the present work, using alumina, silica, and titanium dioxide as the nanoparticle materials, quenching experiments were carried out to explore the mechanisms of the rise of T_{MHF} in nanofluids; stainless steel 304 and Inconel 718 were used as the materials of the specimen and distilled water was used as the base liquid. In the experiments, T_{MHF} increased in all the nanofluids but the increasing rate was dependent significantly on the nanoparticle material and the nanoparticle layer thickness. To elucidate the mechanisms of the heat transfer enhancement, the relations of T_{MHF} with the three basic surface parameters of roughness, wettability, and wickability were examined but no clear relationship was found. When the metal specimen of higher thermal conductivity is covered with the nanoparticle layer of lower thermal conductivity, the contact temperature during quenching should decrease and the contact duration would be dependent on the thermal properties and thickness of the nanoparticle layer. Assuming that T_{MHF} rises with an increase in the contact duration, a new model describing the rise of T_{MHF} in the nanofluid was proposed.

Keywords : Quenching, Nanofluid, Nanoparticle layer, Minimum heat flux temperature, Contact temperature, Contact duration, Surface property

1. Introduction

Rapid cooling of high-temperature body is of considerable importance in various industrial applications. In steel manufacturing, cooling rate during quenching process affects the quality of the products significantly (Nishibata and Kojima, 2013). In next-generation nuclear power plants, in-vessel retention (IVR) is often adopted. In this innovative safety system, the reactor vessel is submerged in coolant to keep molten core in the reactor vessel even when severe accident occurs (Rempe et al., 2008; Zhang et al., 2010). Efficient heat removal from the reactor vessel outer wall of high-temperature is crucial to surely achieve IVR.

Nanofluid is the liquid that contains colloidal dispersion of nanometer-sized solid particles. In recent years, good heat transfer performance of nanofluid in comparison with pure liquid is reported in pool boiling (Kim et al., 2006; Kim et al., 2007; Phan et al., 2009; Ahn et al., 2011; Bolukbasi and Dogan, 2011; Okawa et al., 2012; Fan et al., 2015; Watanabe et al., 2018) as well as in quenching (Kim et al., 2009; Kim et al., 2010; Ciloglu and Bolukbasi, 2011). As an application of nanofluid in quenching, Kim et al. (2009) conducted experiments to obtain boiling curves when high-temperature stainless steel spheres and rodlets are immersed in water-based Al_2O_3 nanofluid. The cooling time was much shorter in the nanofluid than in the pure water since T_{MHF} that is the surface temperature at the minimum heat flux point was raised considerably in the nanofluid. It was discussed that the layer of nanoparticles formed on the heat transfer surface improved surface properties to achieve efficient cooling. Kang et al. (2018) explored the effects of surface properties on T_{MHF}. Saturated water was used as the test liquid and specimens of three different surface conditions called CWS

Paper No.20-00527
J-STAGE Advance Publication date : 18 March, 2021
[DOI: 10.1299/mej.20-00527]

(Completely Wettable Surface), RZS (Roughness Zirconium Surface), and BZS (Bare Zirconium Surface) were utilized. It was reported that T_{MHF} was highest for CWS due to liquid-spreading caused by its high capillary wicking performance. Kikuchi et al. (1985; 1986) and Chandratilleke et al. (1989) investigated the influence of surface coating on the cooling rate during quenching. If the heat transfer surface was covered with a layer of low thermal conductivity, the contact surface temperature decreased even if the layer was thin. In view of this, Kikuchi et al. (1985; 1986) developed a quenching model considering the change in the surface contact temperature due to surface coating.

The above literature survey on the quenching phenomenon suggests that acceleration of cooling in nanofluid may be attributed to the changes in the contact surface temperature and/or the surface properties such as roughness, wettability, and capillary wicking. In this study, quenching process of high-temperature metal rodlets is investigated experimentally to explore the mechanisms of the quenching acceleration in the nanofluid. Distilled water is used as the base liquid and alumina (Al_2O_3), silica (SiO_2), and titanium-dioxide (TiO_2) are utilized as the materials of nanoparticles. As discussed above, the layer of nanoparticles is formed on the rodlet surface during quenching in the nanofluid. Thus, to elucidate the mechanisms of the cooling acceleration, the four surface properties of roughness, wettability, wickability and nanoparticle layer thickness are measured. Based on the experimental results accumulated in this work, discussion is made on the possible mechanisms causing the cooling acceleration in the nanofluid.

2. Experimental descriptions

2.1 Nanofluids

Water-based nanofluids were used as the test liquids. Alumina (Al_2O_3, Aeroxide Alu C), Silica (SiO_2, Aeroxide 90G), and Titanium-dioxide (TiO_2, Aeroxide TiO_2 P25; mixture of 80% anatase and 20% rutile) were selected as the nanoparticle materials. To prepare the nanofluid, 400 mg of nanoparticles were weighed using an electronic balance accurate to within ±0.07 mg (HR-202i, A&D Co., Ltd.). The weighed nanoparticles were then excited in 200 ml of distilled water using an ultrasonic bath (QR-003, Kaijo Co., Ltd.) at 430 kHz for 3 hours to achieve uniform dispersion (Nakamura et al., 2011). Then, distilled water was added to make the total liquid volume 1 liter. Hence, the mass concentration of the nanoparticles was calculated at 0.4 kg/m^3. Figure 1 depicts the appearance of the three nanofluids. The TiO_2 nanofluid was white in color while Al_2O_3 and SiO_2 nanofluids were transparent. The primary particle size reported by the manufacturer was 13 nm for Al_2O_3, 20 nm for SiO_2, and 21 nm for TiO_2, but the mean particle size in the nanofluids measured using the particle analyzer (Otsuka Electronics, FPAR-1000) was 108 nm for Al_2O_3, 234 nm for SiO_2, and 107 nm for TiO_2, suggesting that the nanoparticles formed clusters in the nanofluids. From the mass concentration and the particle size, the number density of primary particles was calculated 8.9×10^{19} m^{-3} for Al_2O_3, 3.7×10^{19} m^{-3} for SiO_2, and 1.8×10^{19} m^{-3} for TiO_2, respectively.

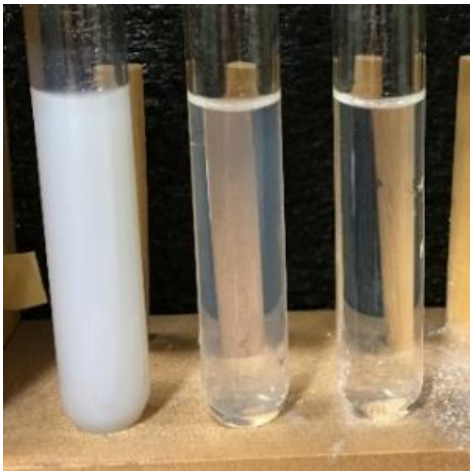

Fig. 1 Photo of nanofluids used in the present experiments (titanium dioxide, alumina, and silica from the left side).

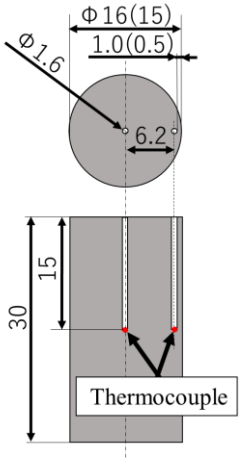

Fig. 2 Geometries of the Inconel 718 specimen (values in parentheses are for the SUS304 specimen) [unit: mm].

2.2 Specimens

Figure 2 shows the geometries of the Inconel 718 and SUS304 rodlets used as the specimens in this work. Inconel 718 rodlet was 16 mm in diameter and 30 mm in length and the SUS304 rodlet was 15 mm in diameter and 30 mm in

[DOI: 10.1299/mej.20-00527]

length. Important properties of Inconel 718 and SUS304 are presented in Table 1. To measure the temperature transient during quenching, two type-K thermocouples (1.6 mm in outer diameter and 0.5s in time constant) were placed in the rodlets as delineated in Fig. 2. One was placed at the center as the typical position to understand the temperature transient qualitatively and the other was placed near the wall to reduce the error in the inverse analysis. The measurement uncertainty of the thermocouples was ±2.5 K for the temperature range of $T < 333$ºC and ±0.75% for $T > 333$ºC. After inserting the thermocouple into the hole, the area surrounding the hole was hit with a sharp-tip tool to fix the thermocouple in the hole. Before the experiment, the rodlet surface was polished using metal polishing paste and then cleaned using acetone and distilled water.

Table 1 Properties of test piece materials (Hernando et al., 2018; Ye et al., 2015)

	Density ρ [kg/m^3]	Thermal conductivity λ [W/m·K]	Specific heat c [J/kg·K]	Thermal diffusivity α [mm^2/s]
Inconel 718				
25°C	8190	8.9	435	2.5
1000°C	7806	26.7	620	5.52
Ave.	7998	17.8	527.5	4.22
SUS304				
25°C	7920	16	490	4.12
1000°C	7500	28	630	5.9
Ave.	7710	22	560	5.10

2.3 Experimental apparatus and procedure

The experiment set up is shown schematically in Fig. 3. The experimental steps are described as follows.

1. A glass cylindrical beaker (133 mm in diameter and 185 mm in height) containing 1 liter of test liquid was put on a hot plate to heat the liquid to 80±1ºC.
2. The rodlet was heated to 1000±2°C in an electronic furnace.
3. The rodlet was immersed in the test liquid to cool the rodlet to the liquid temperature. The process of phase change around the rodlet was recorded using a high-speed camera (FASTCAM mini UX50, Photron Co., Ltd.). The initial temperature difference between the center and periphery thermocouples was within 1K. The rodlet was held vertically in the pool manually; the inclination of the rodlet from the vertical was estimated within 3°.
4. The experimental steps 2 and 3 were repeated five times.

The temperature data measured using the thermocouples were recorded every 0.1s during the experiment. In the observation using the high-speed camera, the spatial resolution was set to 100μm/pixel, the frame rate was 500 frames/s, and the shutter speed was 200μs.

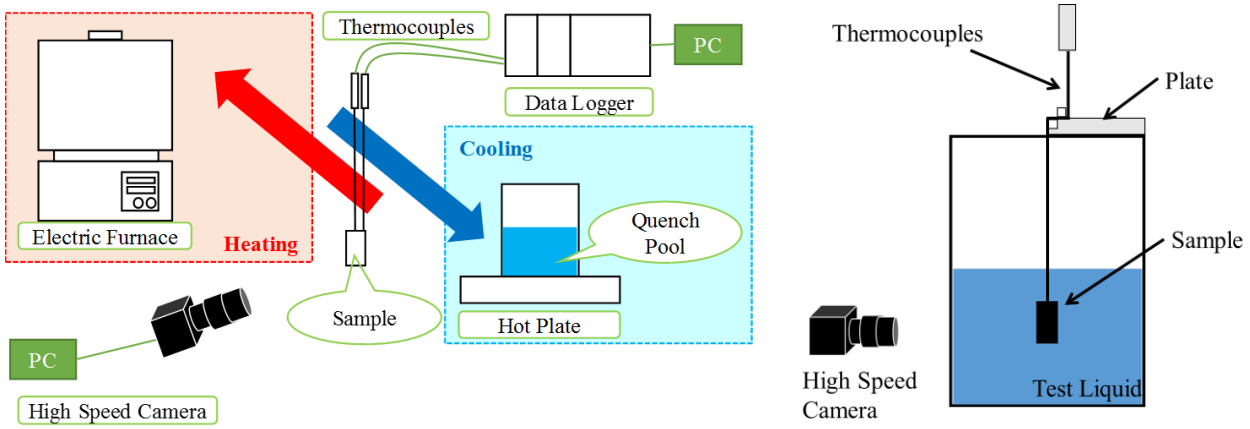

(a) Experimental apparatus and procedure (b) Posture and hold method of rodlet

Fig. 3 Experiment set up.

[DOI: 10.1299/mej.20-00527]

2.4 Calculation methods of wall superheat and wall heat flux

An inverse heat conduction problem was solved to deduce the time variations of the wall superheat and the wall heat flux during quenching. The governing equation was the following one-dimensional heat conduction equation in cylindrical coordinates.

$$\frac{1}{\alpha}\frac{\partial T}{\partial t}=\frac{1}{r}\frac{\partial}{\partial r}\left(r\frac{\partial T}{\partial r}\right) \tag{1}$$

where t is the time, r is the spatial coordinate in the radial direction, T is the temperature, and α is the thermal diffusivity of the rodlet. The thermal properties of the test piece materials were assumed constant at the average values in Table 1 in the calculation. The difference of the calculated minimum heat flux temperature was within 5K even when the properties at 25 and 1000°C were used. The above equation was solved using the Laplace transformation technique (Monde et al., 2003a, 2003b; Woodfield et al., 2006a, 2006b). The initial and boundary conditions are expressed by

$$T|_{t=0}=T_0 \tag{2}$$

$$T|_{r=r_1}=T_1(t)=T_0+\sum_{k=0}^{N_k}\frac{P_{k,1}t^{k/2}}{\Gamma\left((k/2)+1\right)} \tag{3}$$

$$T|_{r=r_2}=T_2(t)=T_0+\sum_{k=0}^{N_k}\frac{P_{k,2}t^{k/2}}{\Gamma\left((k/2)+1\right)} \tag{4}$$

where T_0 is the initial rodlet temperature, r_1 and r_2 are the thermocouple positions in the radial direction, Γ is the gamma function, and N_k is the number of terms of polynomial approximation. The value of N_k was set to 5 and the values of the coefficients $P_{k,1}$ and $P_{k,2}$ were determined by approximating the temperature histories measured at the two thermocouple positions using the least squares method (Woodfield et al., 2006a). The uncertainties in the calculated boiling curves were estimated from the uncertainties of the measured temperature values and radial positions of the thermocouples (±0.4 mm) by changing these values in the inverse analysis. As a result, the uncertainties due to temperature value were estimated less than ±8 K for the wall superheat and ±0.6% for the wall heat flux. Those due to the thermocouple position were estimated less than ±10 K for the wall superheat and ±20% for the wall heat flux. Adding these values, the uncertainties in the calculated boiling curves were estimated less than ±18 K for the wall superheat and 21% for the wall heat flux. Another important factor that induces uncertainty in the calculated boiling curves is the elimination of multidimensional effect in the inverse analysis. As discussed later, quenching first occurred at the bottom of the rodlet in distilled water and in the first run in nanofluid. In consequence, heat transfer in the vertical direction might have a noticeable influence on the calculated boiling curves in these cases. Therefore, in the following sections, only qualitative discussion is possible when comparing the boiling curves for these cases with those for the other cases.

3. Results and discussion

3.1 Qualitative descriptions of the results of quenching experiment

Figure 4 shows the experimental results for the Inconel 718 rodlet immersed in the distilled water. Figure 4(a) presents the temperature transients measured at the center (r = 0 mm) and the periphery (r = 6.2 mm) of the rodlet, and Fig. 4(b) the boiling curves calculated by the inverse analysis; here, ΔT_{wall} in Fig. 4(b) refers the wall superheat. It is noted that the boiling curves for ΔT_{wall} < 800K are shown in Fig. 4(b) since the accurate calculation is not possible immediately after immersion of the rodlet. The boiling curves are compared with the following correlations for nucleate boiling heat transfer Eq. (5) by Rohsenow (1952) (C_{sf} = 0.014), critical heat flux Eq. (7) by Zuber (1958), minimum heat flux point Eq. (8) by Dhir and Purohit (1978), and film boiling heat transfer Eq. (9) by Bromley (1950).

[DOI: 10.1299/mej.20-00527]

$$h_{nucleate} = \frac{\lambda_l}{L_a}\frac{Pr^{-0.7}}{C_{sf}}\left(\frac{qL_a}{\rho_v v_l L_{lv}}\right)^{0.67}\left(\frac{\rho_v}{\rho_l}\right)^{0.67} \tag{5}$$

$$L_a = \sqrt{\frac{\sigma}{g(\rho_l - \rho_v)}} \tag{6}$$

$$q_{CHF} = 0.131\rho_v L_{lv}\left\{\frac{\sigma g(\rho_l - \rho_v)}{\rho_v^2}\right\}^{\frac{1}{4}} \tag{7}$$

$$\Delta T_{MHF} = 101 + 8\Delta T_{sub} \tag{8}$$

$$h_{film} = 0.943\left\{\frac{g\rho_v(\rho_l - \rho_v)\lambda_v^3(L_{lv} + \frac{c_v\Delta T_{wall}}{2})}{\mu_v \Delta T_{sat} l}\right\}^{\frac{1}{4}} \tag{9}$$

where the subscripts l and v denote liquid and vapor phases, respectively, q is the heat flux, L_a is the Laplace length, Pr is Prandtl number, L_{lv} is latent heat of vaporization, C_{sf} is an empirical constant determined by the combination of liquid and heat transfer surface, v is kinematic viscosity, ΔT_{sub} is subcooling, μ is viscosity, l is the height of the thermocouple position from the bottom of test piece, σ is the surface tension, and g is the gravitational acceleration. The film boiling heat transfer coefficient and CHF agree with Bromley's and Zuber's correlations fairly well, respectively. However, noticeable discrepancy with the previous correlations is seen for the experimental values of ΔT_{MHF} and nucleate boiling heat transfer coefficient. These would be attributed to the one-dimensional approximation adopted in the inverse analysis. Four snapshots during quenching are displayed in Figs. 5(a)-(d). In Fig. 5(e), the blue curve denotes the wall temperature history and the gray line shows the heat flux history in the second run calculated by the inverse analysis. As shown in Fig. 5(a), the rodlet was first covered by the vapor film. The vapor film then disappeared gradually from the bottom of the rodlet (Figs. 5(b)-(d)). The lower edge of the vapor film reached the center of the rodlet at about 30s (Fig. 5 (c)). At this moment, the cooling rate is nearly highest value as can be seen in Fig. 5(e). The maximum heat flux was measured when the vapor film disappeared at the thermocouple elevation (Figs. 5(d) and (e)). Figures 4(a) and (b) also indicate that the temperature transient did not change noticeably even if the quenching experiment was repeated.

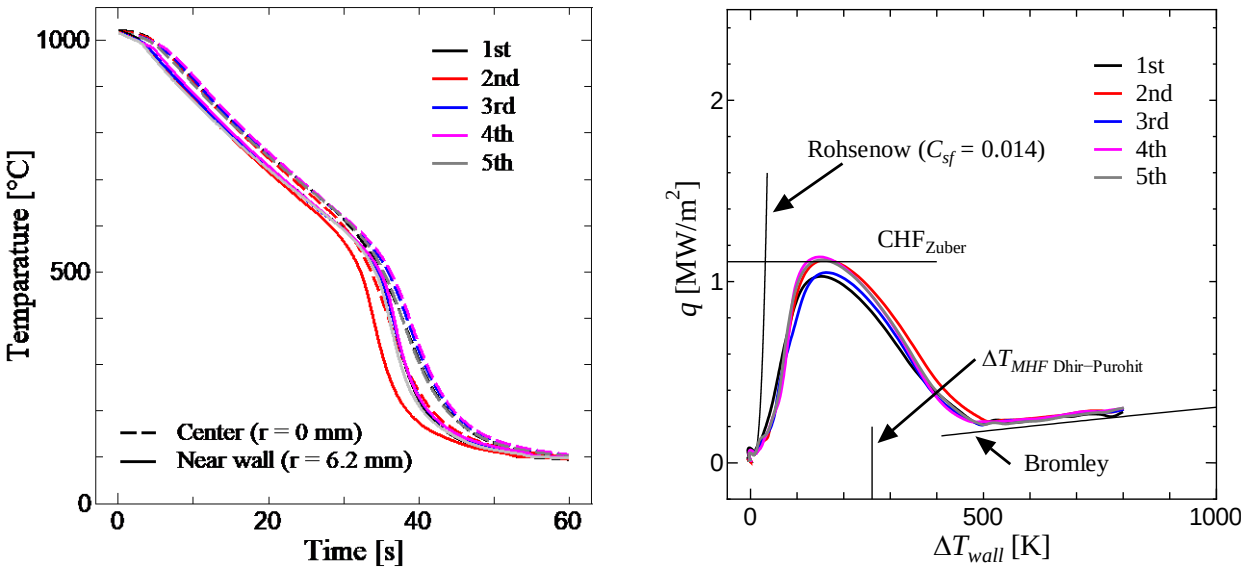

(a) Cooling curves (b) Boiling curves

Fig. 4 Quenching characteristics of high-temperature test piece in distilled water.

[DOI: 10.1299/mej.20-00527]

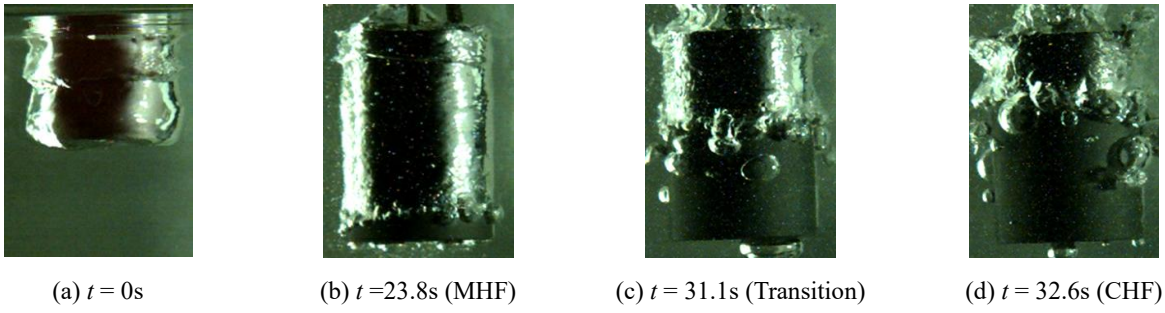

(a) t = 0s (b) t =23.8s (MHF) (c) t = 31.1s (Transition) (d) t = 32.6s (CHF)

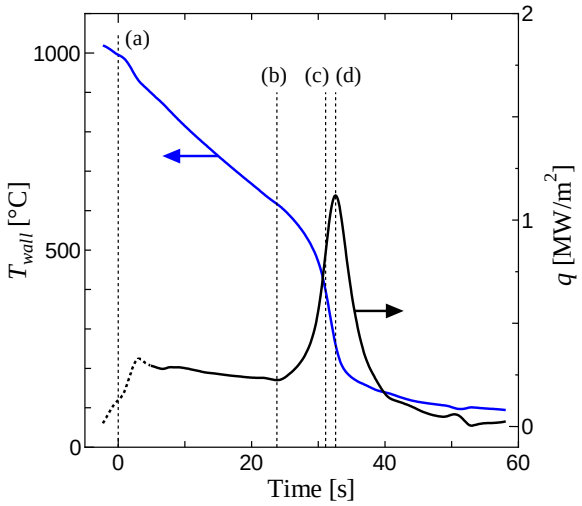

(e) Wall temperature and heat flux history

Fig. 5 Boiling phenomenon during quenching of high-temperature rodlet in distilled water (second run).

The results of temperature measurement and visualization for the Inconel 718 rodlet immersed in the silica nanofluid are presented in Figs. 6 and 7, respectively. Figures 6(a) and (b) indicate that the cooling characteristics in the first run were similar to those in the distilled water, but the cooling performance was improved asymptotically in the subsequent runs. In particular, the wall superheat at the minimum heat flux point ΔT_{MHF} (= $T_{MHF} - T_{sat}$) where the cooling acceleration starts is about 600K in the first run and rose drastically to 800-900K in the subsequent runs (the calculation method of ΔT_{MHF} is described in the appendix). It is also interesting to note that in Fig. 6(b), two clear peaks are seen in the boiling curves in the subsequent runs. The visualization results in the second run are depicted in Fig. 7(a)-(f) and the calculated transients of the wall temperature and heat flux are presented in Fig. 7(g). Figures 7(a) and (b) indicate that the whole surface of the rodlet was first covered by the vapor film as in distilled water but then covered by many small bubbles (Figs. 7(c) and (d)). This distinct boiling mode causes the first peak in the right of the boiling curve and the drastic increase of ΔT_{MHF}. The lower edge of the vapor film then moved upward (Figs. 7(e) and (f)) as observed in the distilled water. The second peak in the left of the boiling curve in Fig. 6(b) can hence be attributed to the collapse of the vapor film as in the case of distilled water.

The cooling curves measured for the Inconel 718 rodlet immersed in Al_2O_3 and TiO_2 nanofluids are presented in Figs. 8(a) and (b), respectively. The cooling time became shorter with repeating the experimental run gradually as in the case of SiO_2 nanofluid. Figures 8(c) and (d) show the calculated boiling curves. The boiling curves for the Al_2O_3 nanofluid are similar to those for the SiO_2 nanofluid. However, in the TiO_2 nanofluid, reduction of ΔT_{MHF} was less significant and the boiling curves are similar to those for the distilled water.

The photos of specimen taken after the fifth run are presented in Fig. 9. The rodlet surface was kept clean even after the experiments for the distilled water (Fig. 9(a)), while the nanoparticle layer was formed in the experiments using the nanofluids (Figs. 9(b)-(d)). The acceleration of cooling might hence be attributed to the modification of the surface properties caused by the nanoparticle deposition. Since the deposition of nanoparticles occurs during nucleate boiling (Saeid and Borca-Tasciuc, 2014; Kwark et al., 2010), it is considered that even in the experiments in nanofluid, the nanoparticle layer was not present on the surface until the wall superheat decreased sufficiently in the first run. This is consistent with the fact that no significant improvement of the cooling rate was observed in the first run in Figs. 6 and 8.

[DOI: 10.1299/mej.20-00527]

It is noted that the nanoparticle layer was yellow in color in Fig. 9(d). This would indicate that chemical reaction of titanium-dioxide with Inconel 718 occurred during quenching to produce titanium-yellow in the TiO_2 nanofluid (Choquette and Trusell, 1978).

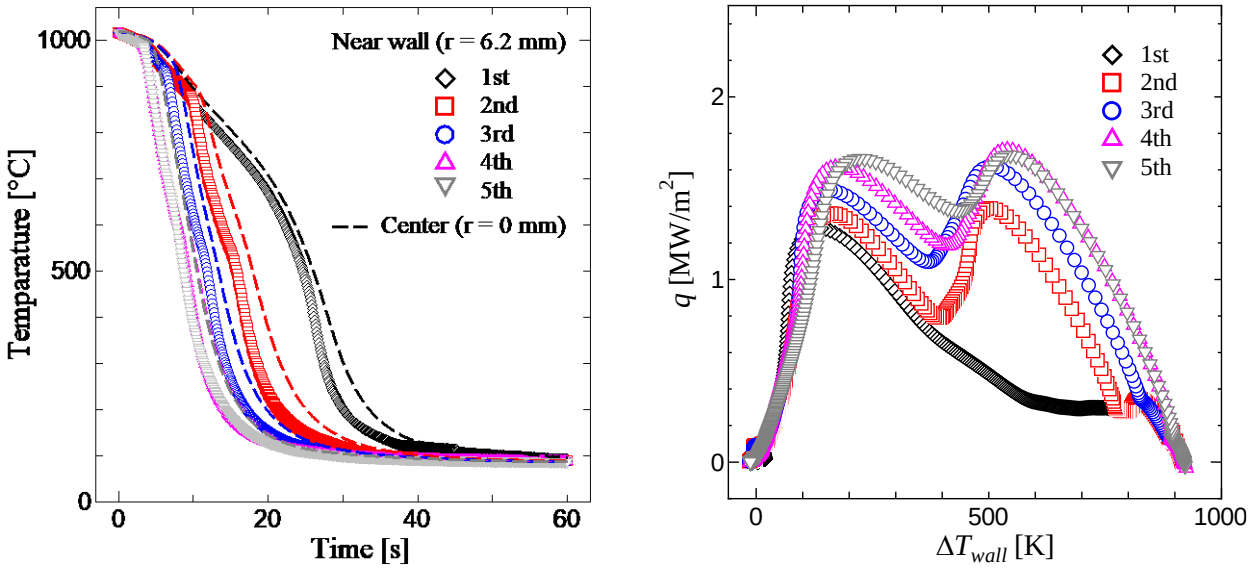

(a) Cooling curves (b) Boiling curves

Fig. 6 Cooling characteristics during quenching of high-temperature test piece in silica nanofluid.

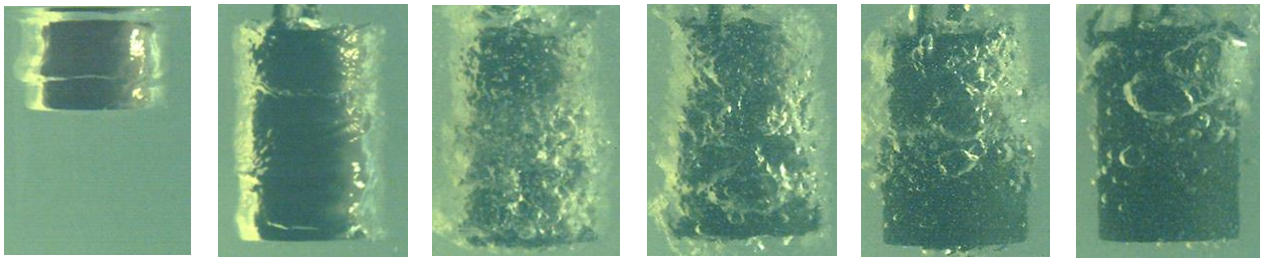

(a) t = 0s (b) t = 6.3s (1st MHF*) (c) t = 8.3s (Transition) (d) t = 9.5s (1st heat flux peak) (e) t = 12.6s (2nd MHF*) (f) t = 15.1s (2nd heat flux peak (=CHF))

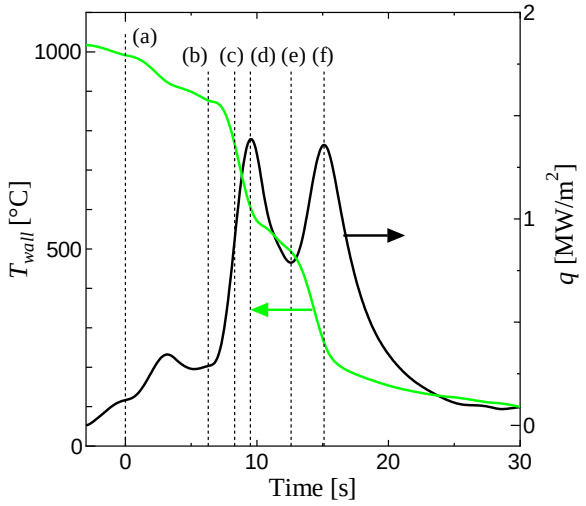

(g) Wall temperature and heat flux history

Fig. 7 Boiling phenomenon during quenching of high-temperature rodlet in silica nanofluid (second run). (*)1st MHF indicates the ordinary MHF corresponding to boiling transition from film boiling to transition boiling.

[DOI: 10.1299/mej.20-00527]

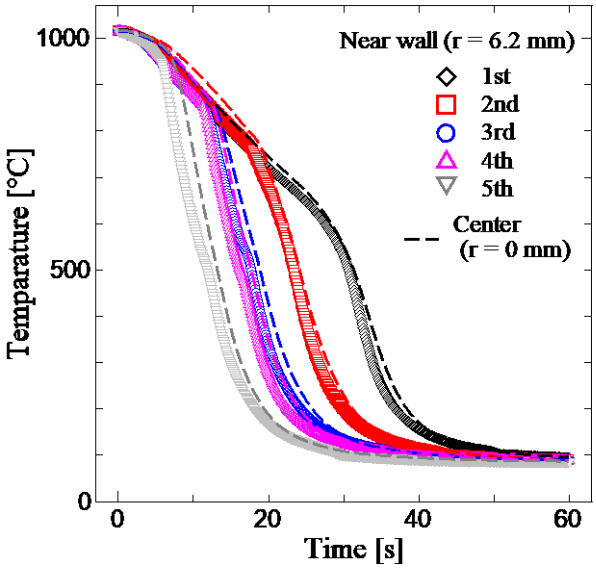

(a) Cooling curves in alumina nanofluid

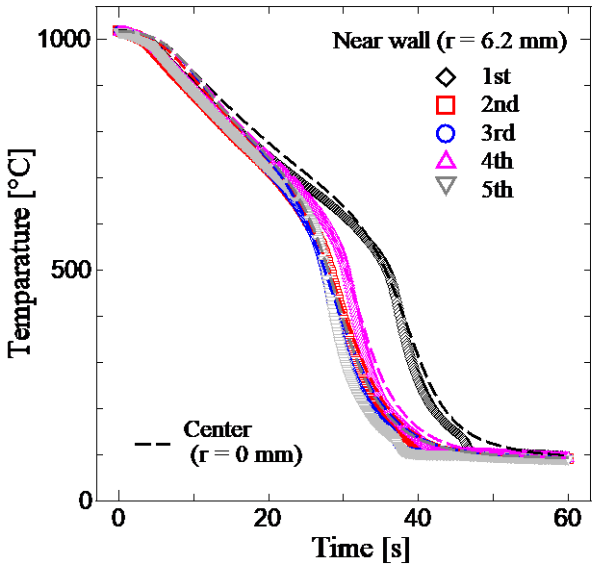

(b) Cooling curves in titanium dioxide nanofluid

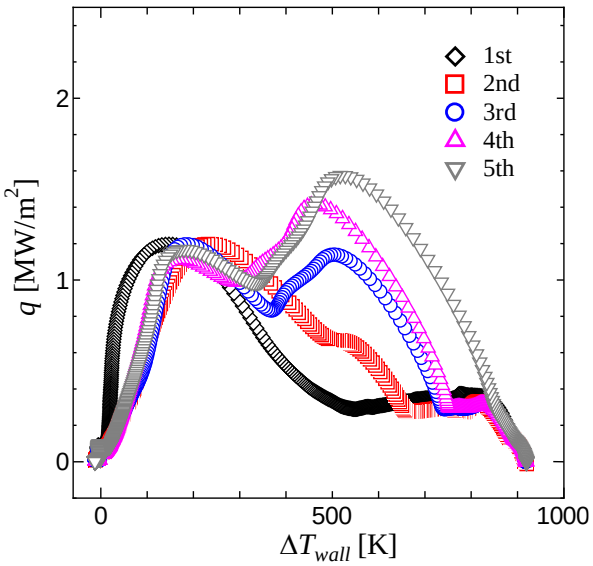

(c) Boiling curves in alumina nanofluid

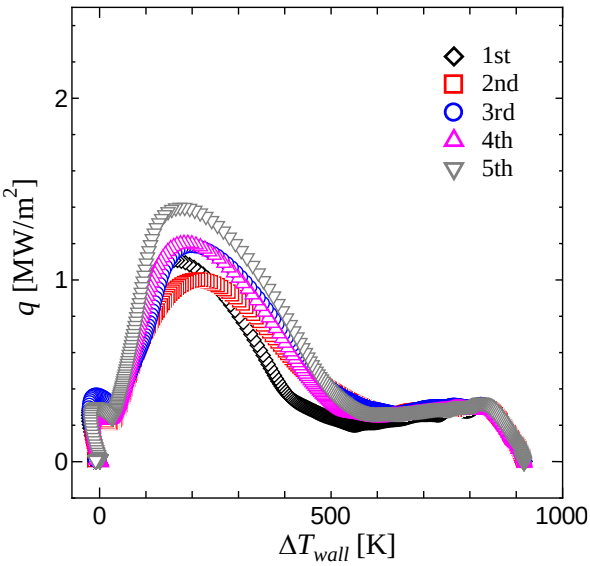

(d) Boiling curves in titanium dioxide nanofluid

Fig. 8 Cooling and boiling curves in different nanofluids.

(a) Distilled water (b) Silica nanofluid (c) Alumina nanofluid (d) Titanium dioxide nanofluid

Fig. 9 Photos of the test piece taken after the 5th run.

[DOI: 10.1299/mej.20-00527]

3.2 Effects of surface properties on T_{MHF}

The cooling and boiling curves in Figs. 4, 6 and 8 indicate that the improvement of cooling rate in nanofluids is mainly attributed to the increase of T_{MHF}. Thus, the mechanism to cause the rise of T_{MHF} is explored in the followings.

Kim et al. (2010) indicated that the surface roughness promotes solid-liquid contact at high temperature to increase T_{MHF} during quenching. Thus, the average surface roughness Sa was measured using a 3D laser scanning confocal microscope and the relation of Sa and ΔT_{MHF} are presented in Fig. 10; here, the symbols and error bars show the average and the range of measurements of Sa at eight locations, respectively. It can be seen that in comparison with the Inconel 718 surface after quenching in water, the values of Sa after quenching in nanofluids are greater. In addition, the value of Sa tends to increase with repeating the experimental runs. It is also seen that ΔT_{MHF} tends to increase with an increase in Sa. To confirm the dependency of ΔT_{MHF} on Sa, the same experiment was done using two SUS304 rodlets: one was the normal rodlet without surface treatment and the other was polished with sandpaper to roughen its surface. The results for these two rodlets are also presented in Fig. 10. In the quenching experiment immersing the roughened SUS304 rodlet in water, the surface roughness was largest (Sa = 7.7 μm) but the minimum heat flux temperature was maintained low (ΔT_{MHF} = 524K). This indicates that the surface roughness may have noticeable influence on ΔT_{MHF} but the increase of ΔT_{MHF} measured in this work cannot be attributed solely to the surface roughness.

Kang et al. (2018) explored the effects of surface wettability on ΔT_{MHF} experimentally to conclude that ΔT_{MHF} is higher for the surface of low contact angle. Thus, to test the effect of surface wettability, the contact angle of the rodlet surface θ was measured using a contact angle goniometer (PG-X, Fibro System AB). The relation between ΔT_{MHF} and θ is presented in Fig. 11. The value of θ was 75±10° in the experiments using distilled water. However, for the surfaces after quenching in nanofluids, the value of θ was measured zero since droplets were absorbed in the nanoparticle layer formed on the surface. Thus, increasing trend of ΔT_{MHF} with a decrease in θ is seen in Fig. 11, but it is not possible to express the dependence of ΔT_{MHF} on the properties of nanoparticle layer as a function of θ.

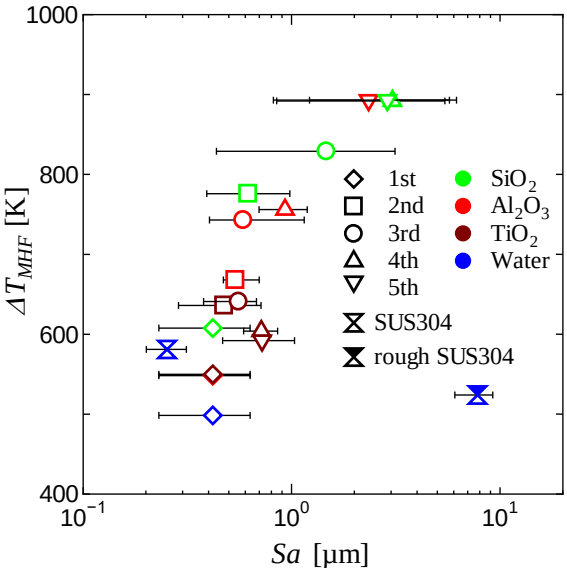

Fig. 10 Effect of surface roughness Sa on ΔT_{MHF}.

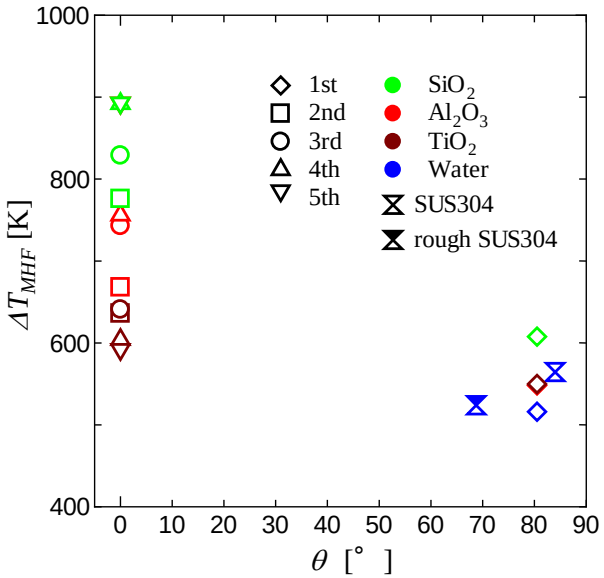

Fig. 11 Effect of wettability on enhancement of ΔT_{MHF}.

Rahman et al. (2014) used the wickability that expresses capillary wicking performance of the heat transfer surface to correlate the critical heat flux in pool boiling. The surface wickability Wi was quantified using the liquid volume wicked into the surface per unit time. In this work, by reference to Rahman et al. (2014), Wi was determined as follows.

(1) The tip of distilled water kept in a capillary tube of 1.04 mm in inner diameter was touched with the surface.
(2) The water was absorbed in the nanoparticle layer by wicking action. The liquid volume wicked per unit time was determined from the change in the water level in the capillary tube.
(3) From the volumetric flux of the wicked liquid $\dot{V}_0''$, the wickability Wi was calculated by

[DOI: 10.1299/mej.20-00527]

$$Wi = \frac{\dot{V}_0'' \rho_l}{\rho_g^{1/2}\left[\sigma g(\rho_l - \rho_g)\right]^{1/4}} \tag{10}$$

$$\dot{V}_0'' = \frac{1}{A_w}\left(\frac{dV}{dt}\right)_{t=0} \tag{11}$$

where the subscript g denotes gas phases, respectively, $(dV/dt)_{t=0}$ is the initial volume flow rate, A_w is the cross-sectional area of the capillary tube. Li et al. (2019) reported that the transitional heat flux during quenching is enhanced with an increase in the modified Weber number that is equivalent to the square of *Wi*. Based on this result, they discussed that the wicking performance of the surface influenced the vapor film behavior and transitional heat flux in their experiments. It is therefore probable that the surface wickability affected the value of ΔT_{MHF} in the present experiments. In view of this, the relation of *Wi* and ΔT_{MHF} is explored in Fig. 12; here, the symbols and error bars show the average and the range of twelve-times measurements of *Wi*, respectively. It can be seen that in the SiO_2 and Al_2O_3 nanofluids, the value of *Wi* is fairly constant but ΔT_{MHF} tends to increase with repeating the experiment. In the TiO_2 nanofluid, *Wi* increases with the experimental run but the value of ΔT_{MHF} is fairly constant. It seems that surface wickability is not the main cause of the heat transfer enhancement measured in this work.

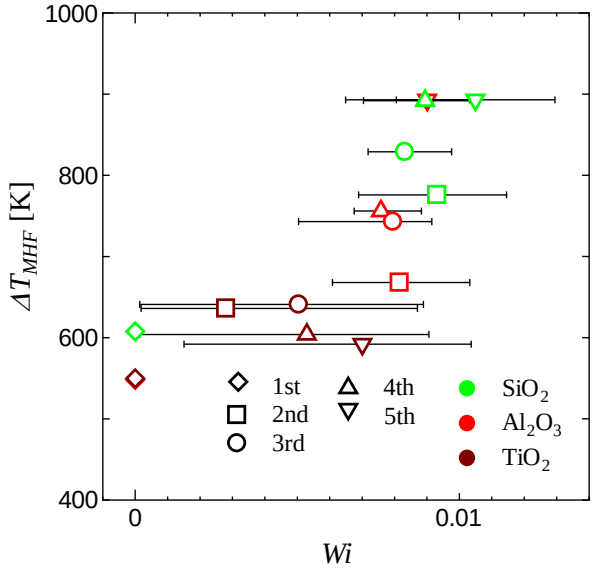

Fig. 12 Effect of wickability on enhancement of ΔT_{MHF}.

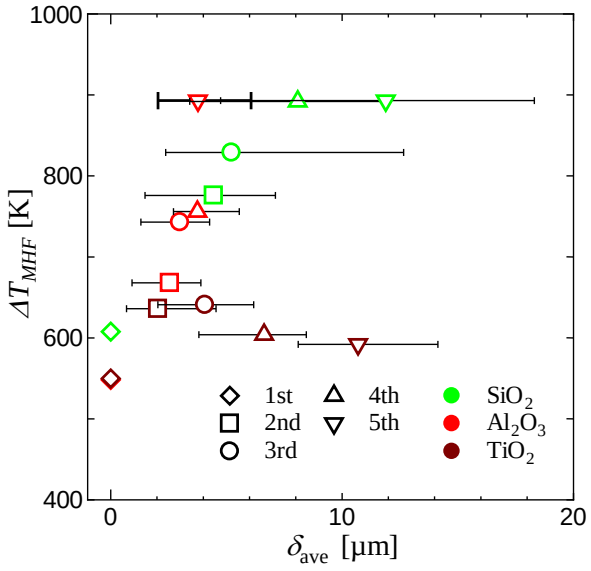

Fig. 13 Effect of average nanoparticle layer thickness on enhancement of ΔT_{MHF}.

3.3 Effects of the low-thermal-conductivity layer on the heat transfer surface

The investigation in the previous section suggests that in contrast to the previous studies, the heat transfer enhancement for the nanoparticle-deposited surfaces observed in the present experiments may not mainly be attributed to the modification of surface properties such as roughness, wettability and wickability.

It is generally accepted that in film boiling, a high temperature surface is covered totally by a vapor film (Incropera et al., 2007). Bradfield (1963), Yao and Henry (1978) and Kikuchi et al. (1992) however indicated that instantaneous liquid-solid contact occurs even in the film boiling. Kikuchi et al. (1985, 1986) further discussed the possibility that the low-thermal-conductivity layer formed on the heat transfer surface causes early collapse of a vapor film during quenching. They developed an intermittent liquid-solid contact model to describe the rise of ΔT_{MHF} for the specimens coated with the low-thermal-conductivity layer. The model postulates that the liquid-solid contact process during film boiling can be divided into three periods: dry, conduction, and evaporation periods. The wall temperature transient during each of the three periods is calculated using the one-dimensional heat conduction equation in cylindrical coordinates Eq. (1). The boundary condition on the layer surface is different in each period as shown below.

I. Dry period ($t < 0$)

Before the occurrence of instantaneous liquid-solid contact, cooling mechanism of the high temperature specimen

[DOI: 10.1299/mej.20-00527]

is pure film boiling. Denoting the film boiling heat transfer coefficient by h_{fb}, the boundary conditions are given by

at $r = 0$

$$\frac{\partial T}{\partial r} = 0 \tag{12}$$

at $r = R$

$$\lambda_{sp} \left.\frac{\partial T}{\partial r}\right|_{sp} = \lambda_{layer} \left.\frac{\partial T}{\partial r}\right|_{layer} \tag{13}$$

$$T_{sp} = T_{layer} \tag{14}$$

at $r = R + \delta$

$$-\lambda_{layer} \frac{\partial T}{\partial r} = h_{\mathrm{fb}}(T - T_{sat}) \tag{15}$$

where R is the radius of cylindrical specimen, δ is the layer thickness, T_{sat} is the saturation temperature, and the subscripts *sp* and *layer* denote the specimen and layer, respectively.

II. Conduction period ($0 \le t < \tau_{\mathrm{c}}$)

It is supposed that the coolant touches the surface of high-temperature specimen but phase change does not occur during the conduction period. The heat transfer mechanism within this period is heat conduction and the boundary condition on the layer surface is replaced by

at $r = R + \delta$

$$T - T_{sat} = \frac{T_{sp} - T_{sat}}{\left(1 + \dfrac{h_{\mathrm{fb}}\delta}{\lambda_{layer}}\right)\left(1 + \sqrt{\dfrac{\rho_l c_l \lambda_l}{\rho_{layer} c_{layer} \lambda_{layer}}}\right)} \tag{16}$$

where the subscript *l* denotes the coolant.

III. Evaporation period ($\tau_{\mathrm{c}} \le t \le \tau_{\mathrm{c}} + \tau_{\mathrm{e}}$)

Evaporation commences at $t = \tau_{\mathrm{c}}$ and continues for the period of τ_{e}. The boundary condition on the layer surface is hence given by

at $r = R + \delta$

$$-\lambda_{layer} \frac{\partial T}{\partial r} = q_e \tag{17}$$

where q_{e} denotes the evaporation heat flux.

Table 2 Parameters used in the Kikuchi model (Kikuchi et al., 1986)

Parameter	
h_{fb} [W/m^2·K]	280
ΔT_{iso} [K]	130
q_e [W/m^2]	1.5×10^6
τ_e [ms]	50
τ_c [ms]	10

The heat conduction equation (Eq. (1)) is discretized based on the finite-difference method to calculate the temperature transient using fully-implicit scheme for time integration. It is supposed that if the superheat of the layer

[DOI: 10.1299/mej.20-00527]

surface becomes lower than the critical value ΔT_{iso}, the film boiling is finished and the transition boiling begins. The values of h_{fb}, ΔT_{iso}, q_e, τ_e and τ_c recommended by Kikuchi et al. (1986) are listed in Table 2.

In our quenching experiments using nanofluids, the rodlets were covered with the layer of nanoparticles. The average nanoparticle layer thickness was within 2−12μm as presented in Fig. 13. Since the thermal conductivities of nanoparticle materials were lower than that of Inconel 718, the situation is similar to that supposed by Kikuchi et al. (1985, 1986). Thus, it is also probable that the improvement of ΔT_{MHF} measured in this work can be described using Kikuchi et al.'s model. It should however be noted that evaluation of the nanoparticle layer properties is not simple since it has porous structure. The method to estimate the properties of the nanoparticle layer used in this work is described as follows. First, the nanoparticle layer density ρ_{nl} is calculated simply from its mass and volume by

$$\rho_{nl} = \frac{m}{\pi L\{(R+\delta_{ave})^2 - R^2\}} \tag{18}$$

where m is the total mass of nanoparticle layer, δ_{ave} is the average nanoparticle layer thickness, and L is the length of the rodlet. Using ρ_{nl}, porosity of the nanoparticle layer ε is determined by

$$\varepsilon = \frac{\rho_n - \rho_{nl}}{\rho_n} \tag{19}$$

where the subscript n denotes the nanoparticle material. It was assumed that the pore of the nanoparticle layer was filled with water vapor during film boiling before ΔT_{MHF} is reached. The effective specific heat of the nanoparticle layer c_{layer} is hence estimated as a function of ε as

$$A = \frac{\varepsilon\rho_v}{\varepsilon\rho_v + (1-\varepsilon)\rho_n} \tag{20}$$

$$c_{nl} = Ac_v + (1-A)c_n \tag{21}$$

where the subscript v denotes the water vapor. Finally, the effective thermal conductivity of the nanoparticle layer λ_{nl} is calculated by

$$\lambda_{nl} = \varepsilon\lambda_v + (1-\varepsilon)\lambda_n \tag{22}$$

To calculate the value of ρ_{nl} for each nanoparticle material by Eq. (18), δ_{ave} was measured using the laser microscope after four-times quenching; then, the nanoparticle layer was removed from the rodlet with a spatula to measure m using the electronic balance. The thermal properties of SiO_2, Al_2O_3 and water vapor are presented in Table 3; here, the thermal properties of nanoparticle materials and water vapor were referred to Refs. (JSME, 1986, Lemmon et al., 2018), respectively. As for TiO_2, it was changed to titanium yellow whose thermal properties are unknown during the experiment. Thus, the properties of TiO_2 are not included in Table 3 and its experimental results are not used in the following analyses. The calculated thermal properties of the nanoparticle layers are presented in Table 4. It can be confirmed that the estimated thermal conductivities of the nanoparticle layers are much lower than that of the rodlet material.

Table 3 Properties of the nanoparticle layer materials (JSME, 1986) and water vapor (Lemmon et al., 2018)

	Density ρ [kg/m^3]	Thermal conductivity λ [W/m･K]	Specific heat c [J/kg･K]	Weight m [mg]	Porosity ε [-]
SiO_2	2580	3.06	1225	0.75	0.983
Al_2O_3	3926	13	1181	0.47	0.978
Vapor (water) at 550°C	0.26	0.072	2168	–	–

[DOI: 10.1299/mej.20-00527]

The temperature transients at the nanoparticle layer surface calculated using Kikuchi et al.'s model is displayed in Fig. 14, where the initial temperature was set to 1000°C as in the experiments. Since the formation of nanoparticle layer occurs during nucleate boiling, it is supposed that the nanoparticle layer was not present on the rodlet surface when ΔT_{MHF} was reached in the first experimental run. Thus, Kikuchi et al.'s model was applied to the subsequent runs. It can be seen in Fig. 14 that the calculated surface temperatures fell far below the critical temperature T_{iso} (= 230ºC) as soon as liquid-solid contact occurs. This implies that the value of T_{MHF} is estimated higher than 1000ºC. In addition, the calculated temperature transient is hardly influenced by the number of experimental runs for each nanofluid. These are not consistent with the present experimental results.

Table 4 Estimated properties of the nanoparticle layers

	Density ρ_{nl} [kg/m^3]	Thermal conductivity λ_{nl} [W/m·K]	Specific heat c_{nl} [J/kg·K]
SiO_2	41.8	0.12	1483
Al_2O_3	82.6	0.34	1306

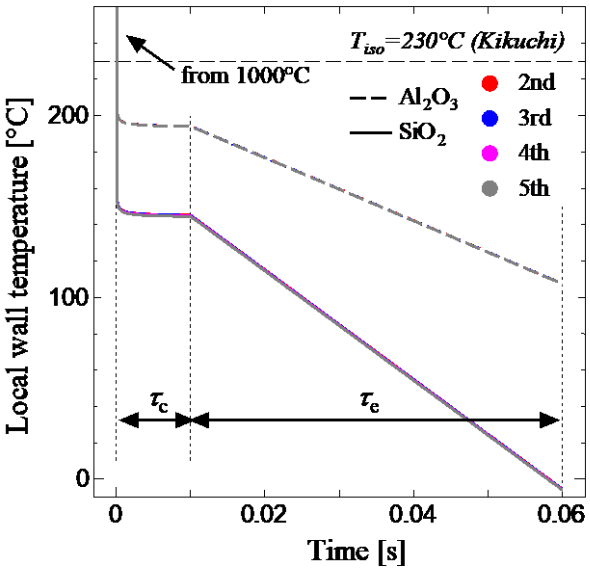

Fig. 14 Temperature transients calculated using Kikuchi et al.'s model.

3.4 Proposal of a new model for T_{MHF}

Since the existing models were not satisfactory to explain the values of T_{MHF} measured in this work, it was tried to develop a new model for quenching of the specimen covered with a thin nanoparticle layer. The new model calculates the temperature histories within the specimen, nanoparticle layer, and the coolant after the nanoparticle layer instantaneously contacts with the coolant. The one-dimensional heat conduction equation in cylindrical coordinates Eq. (1) is used as a governing equation. To derive the temperature transients, Eq. (1) was discretized based on the finite difference method. The central difference scheme was applied to the space-derivative term and the explicit Euler method was used for time integration. The mesh size was set to 0.1 μm and the time step was set so as to satisfy von Neumann's stability condition (Takahashi and Tanamachi, 1991). It was confirmed that mesh-size dependency of the numerical results was sufficiently small. The initial temperature was set to 1000°C in the specimen and the nanoparticle layer and 100°C in water. At the outside boundaries of the regions of specimen and water, the constant temperature conditions of 1000ºC and 100ºC were applied, respectively. As a typical example, Fig. 15 displays the temperature transient at the nanoparticle layer surface calculated for the second run in the silica nanofluid. Here, the nanoparticle layer thickness measured after the first run was used in the simulation assuming that the nanoparticle layer was mainly formed during nucleate boiling in the previous runs. It can be seen that the surface temperature falls rapidly from 1000ºC to 149ºC after the contact. This value is far below the minimum heat flux temperature of 361ºC that is estimated using the widely-accepted correlation by Dhir and Purohit (1978). However, by virtue of the heat supplied from the high-temperature

[DOI: 10.1299/mej.20-00527]

specimen, the surface temperature recovers to 361ºC within a short time period of 0.23ms. Thus, solid-liquid contact would be permitted only for $\tau_c = 0.23$ms in this case. It is considered that to achieve vapor film collapse, solid-liquid contact should be maintained for sufficiently long time for nucleate boiling to occur. Otherwise, local instantaneous solid-liquid contact disappears and the nanoparticle layer surface is covered with the vapor film again. The contact time is dependent on the thermal properties and thickness of the nanoparticle layer. Figure 16 presents the relation between the contact duration τ_c and ΔT_{MHF}, indicating that ΔT_{MHF} tends to increase with an increase in τ_c as expected. However, the trend seems different between the silica and alumina nanofluids. In particular, in the fifth run in the alumina nanofluid, the calculated contact duration is short but the value of ΔT_{MHF} is very high. One of the possible reasons for the different trend is the difference in the porous structure of the nanoparticle layer formed in the silica and alumina nanofluids. The effect of porous structure on the effective thermal properties of the nanoparticle layer and the quenching characteristics should hence be investigated in future studies.

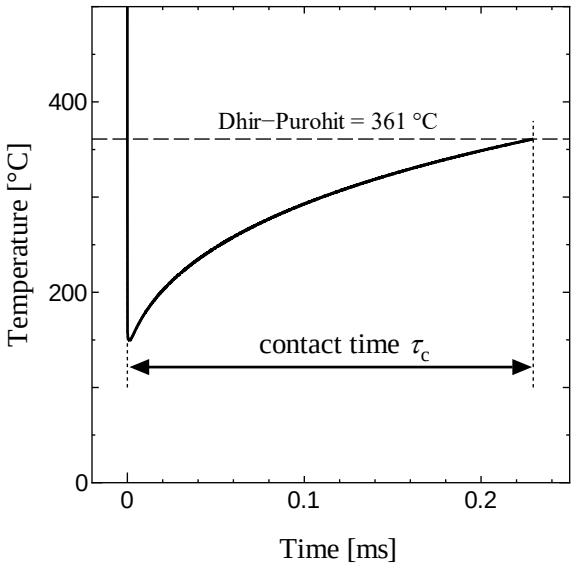

Fig. 15 Temperature history after liquid-solid contact on the silica nanoparticle surface from 1000°C.

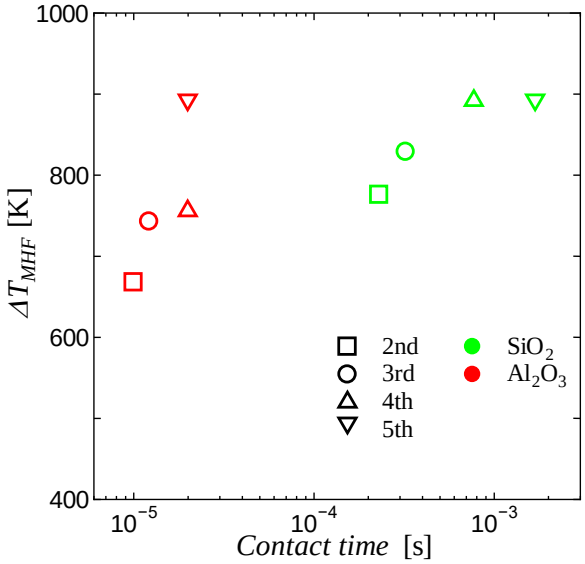

Fig. 16 Effect of contact time on enhancement of ΔT_{MHF}.

4. Conclusion

The minimum heat flux temperature during quenching in nanofluid was studied experimentally using Al_2O_3, SiO_2 and TiO_2 as the nanoparticle materials dispersed in the base liquid. Main conclusions of this work are summarized as follows.

(1) The minimum heat flux temperature rises in nanofluid due to formation of nanoparticle layer on the heat transfer surface during nucleate boiling. The rate of the heat transfer enhancement depends on nanoparticle layer's material and thickness.

(2) No simple dependency of the minimum heat flux temperature enhancement on the surface parameters of the nanoparticle layer (roughness, wettability and wickability) was found. It was also not possible to explain the rise of the minimum heat flux temperature solely from the reduction of the contact temperature caused by the nanoparticle layer of low thermal conductivity.

(3) A new model that describes the rise of the minimum heat flux temperature from the contact duration of the nanoparticle layer with the coolant was proposed. The model succeeded to explain the rise of the minimum heat flux temperature with an increase in the nanoparticle layer thickness. It should however be noted that the rise of the minimum heat flux temperature was not expressed as a single function of the contact duration if the nanoparticle material was different. It was discussed that the porous structure of the nanoparticle layer would be dependent on the nanoparticle material and might have influences on the effective thermal properties of the nanoparticle layer and the process of quenching.

[DOI: 10.1299/mej.20-00527]

Appendix. Calculation method of the minimum heat flux point

The minimum heat flux point was determined using the boiling curve obtained by the inverse analysis. Figure A1 shows the enlarged boiling curves for distilled water presented in Fig. 4(b). In these cases, the wall superheat at the minimum heat flux point ΔT_{MHF} can simply be defined as the value of ΔT_{wall} at the local minimum of the heat flux. However, when rapid temperature reduction occurred at higher temperature, the minimum heat flux point was not obvious. The method to determine ΔT_{MHF} in this case is described in Fig. A2 using the third run in the silica nanofluid as an example. In the experiment, the heat flux was kept increasing as shown in the figure. The temporal derivative of heat flux dq/dt is also plotted in Fig. A2. In this work, the value of ΔT_{wall} at the local minimum point of dq/dt just before the value of dq/dt was kept increasing was regarded as the minimum heat flux point ΔT_{MHF}.

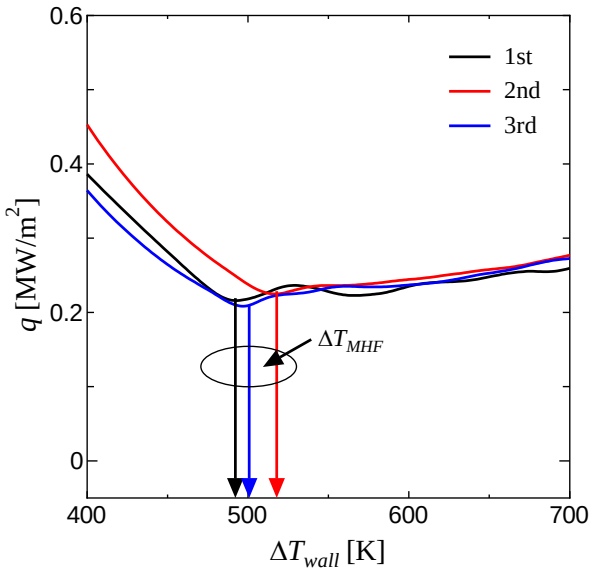

Fig. A1 Boiling curves in distilled water.

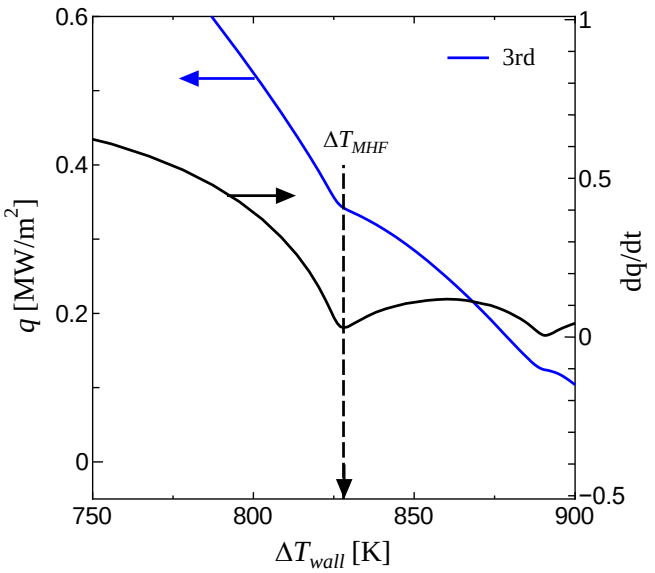

Fig. A2 Boiling curve in silica nanofluid.

Acknowledgment

The authors are very grateful to Dr. Wei Liu (Kyushu Univ.) who gave us fruitful advices for the calculations of wall heat flux and wall superheat using Laplace transformation.

References

Ahn, H.S., Jo, H.J., Kang, S.H., Kim, M.H., Effect of liquid spreading due to nano/microstructures on the critical heat flux during pool boiling, Applied Physics Letters, Vol.98, No.7 (2011), 071908.

Bolukbasi, A., Dogan, C., Pool boiling heat transfer characteristics of vertical cylinder quenched by SiO_2–water nanofluids, International Journal of Thermal Sciences, Vol.50, No.6 (2011), pp.1013-1021.

Bradfield, W.S., Liquid-solid contact in stable film boiling, Industrial & Engineering Chemistry Fundamentals, Vol.5 (1963), pp.200-204.

Bromley, L.A., Heat Transfer in Stable Film Boiling. Chemical Engineering Progress, 46 (1950), pp.221-227.

Chandratilleke, G.R., Nishio, S., Ohkubo, H., Pool boiling heat transfer to saturated liquid helium from coated surface. Cryogenics, Vol.29, No.6 (1989), pp.588-592.

Choquette, P.W., Trusell, F.C., A procedure for making the titan-yellow stain for Mg-calcite permanent, Journal of Sedimentary Research, Vol.48, No.2 (1978), pp.639-641.

Ciloglu, D., Bolukbasi, A., The quenching behavior of aqueous nanofluids around rods with high temperature, Nuclear Engineering and Design, Vol.241, No.7 (2011), pp.2519-2527.

Dhir, V.K., Purohit, G.P., Subcooled film-boiling heat transfer from spheres, Nuclear Engineering and Design, Vol.47, No.1 (1978), pp.49-66.

[DOI: 10.1299/mej.20-00527]

Fan, L.W., Li, J.Q., Li, D.Y., Zhang, L., Yu, Z.T., Cen, K.F., The effect of concentration on transient pool boiling heat transfer of graphene-based aqueous nanofluids, International Journal of Thermal Sciences, Vol.91 (2015), pp.83-95.

Hernando, I., Renderos, M.A., Cortina, M., Ruiz, J.E., Arrizubieta, J.I., Lamikiz, A., Inconel 718 laser welding simulation tool based on a moving heat source and phase change, Procedia CIRP, Vol.74 (2018), pp.674-678.

Incropera, F.P., Dewitt, D.P., Bergman, T.L., Lavine, A.S., Fundamentals of Heat and Mass Transfer, Sixth ed., John Wiley & Sons (2007), Sec.10.3.

JSME data book: Heat transfer ver. 4, JSME, Maruzen, (1986), pp.320.

Kang, J., Kim, T.K., Lee, G.C., Park, H.S., Kim, M.H., Minimum heat flux and minimum film-boiling temperature on a completely wettable surface: effect of the bond number, International Journal of Heat and Mass Transfer, Vol.120 (2018), pp.399-410.

Kikuchi, Y., Hori, T., Michiyoshi, I., Minimum film boiling temperature for cooldown of insulated metals in saturated liquid, International Journal of Heat and Mass Transfer, Vol.28, No.6 (1985), pp.1105-1114.

Kikuchi, Y., Hori, T., Yanagawa, H., Michiyoshi, I., The effect of thin insulating layer on heat transfer characteristics during quenching of hot metals in saturated water, Transactions of the Iron and Steel Institute of Japan, Vol.26, No.6 (1986), pp.576-581.

Kikuchi, Y., Ebisu, T., Michiyoshi, I., Measurement of liquid-solid contact in film boiling, International Journal of Heat and Mass Transfer, Vol.35 (1992), pp.1589-1594.

Kim, H., Kim, J., Kim, M.H., Effect of nanoparticles on CHF enhancement in pool boiling of nano-fluids, International Journal of Heat and Mass Transfer, Vol.49, No.25-26 (2006), pp.5070-5074.

Kim, S.J., Bang, I.C., Buongiorno, J., Hu, L.W., Study of pool boiling and critical heat flux enhancement in nanofluids, Bulletin of the Polish Academy of Sciences: Technical Sciences, Vol.5, No.2 (2007), pp.211-216.

Kim, H., DeWitt, G., McKrell, T., Buongiorno, J., Hu, L.W., On the quenching of steel and zircaloy spheres in water-based nanofluids with alumina, silica and diamond nanoparticles, International Journal of Multiphase Flow, Vol.35, No.5 (2009), pp.427-438.

Kim, H., Buongiorno, J., Hu, L.W., McKrell, T., Nanoparticle deposition effects on the minimum heat flux point and quench front speed during quenching in water-based alumina nanofluids, International Journal of Heat and Mass Transfer, Vol.53, No.7-8 (2010), pp.1542-1553.

Kwark, S.M., Kumar, R., Moreno, G., Yoo, J., You, S.M., Pool boiling characteristics of low concentration nanofluids, International Journal of Heat and Mass Transfer, Vol.53, No.5-6 (2010), pp.972-981.

Lemmon, E.W., Bell, I.H., Huber, M.L., McLinden, M.O., NIST Standard Reference Database 23: Reference Fluid Thermodynamic and Transport Properties-REFPROP, Version 10.0, National Institute of Standards and Technology, Standard Reference Data Program, Gaithersburg (2018).

Li, J.Q., Zhang, J.Y., Mou, L.W., Zhang, Y.H., Fan, L.W., Enhanced transitional heat flux by wicking during transition boiling on microporous hydrophilic and superhydrophilic surfaces, International Journal of Heat and Mass Transfer, Vol.141 (2019), pp.835-844.

Monde, M., Arima, H., Mitsutake, Y., Estimation of surface temperature and heat flux using inverse solution for one-dimensional heat conduction, Journal of Heat Transfer, Vol.125, No.2 (2003a), pp.213-223.

Monde, M., Arima, H., Liu, W., Mitutake, Y., Hammad, J.A., An analytical solution for two-dimensional inverse heat conduction problems using Laplace transform, International Journal of Heat and Mass Transfer, Vol.46, No.12 (2003b), pp.2135-2148.

Nakamura, T., Okawa, H., Kawamura, Y., Sugawara, K., Solid–liquid separation by sonochemistry: A new approach for the separation of mineral suspensions, Ultrasonics Sonochemistry, Vol.18, No.1 (2011), pp.85-91.

Nishibata, T., Kojima, N., Effect of quenching rate on hardness and microstructure of hot-stamped steel, Journal of Alloys and Compounds, Vol.577 (2013), S549-S554.

Okawa, T., Takamura, M., Kamiya, T., Boiling time effect on CHF enhancement in pool boiling of nanofluids, International Journal of Heat and Mass Transfer, Vol.55, No.9-10 (2012), pp.2719-2725.

Phan, H.T., Caney, N., Marty, P., Colasson, S., Gavillet, J., Surface wettability control by nanocoating: the effects on pool boiling heat transfer and nucleation mechanism. International Journal of Heat and Mass Transfer, Vol.52, No.23-24 (2009), pp.5459-5471.

Rahman, M.M., Olceroglu, E., McCarthy, M., Role of wickability on the critical heat flux of structured superhydrophilic surfaces, Langmuir, Vol.30, No.37 (2014), pp.11225-11234.

[DOI: 10.1299/mej.20-00527]

Rempe, J.L., Suh, K.Y., Cheung, F.B., Kim, S.B., In-vessel retention of molten corium: lessons learned and outstanding issues, Nuclear Technology, Vol.161, No.3 (2008), pp.210-267.

Rohsenow, W. M., A method of correlating heat transfer data for surface boiling of liquids, Transactions of ASME, Vol.74, (1952), pp.969-976.

Saeid, V., Borca-Tasciuc, T., Role of nanoparticles on nanofluid boiling phenomenon: Nanoparticle deposition, Chemical Engineering Research and Design, Vol.92, No.5 (2014), pp.842-856.

Takahashi, R., Tanamachi, Y., Finite difference method, Baifukan (1991), Sec. 4.4.

Watanabe, Y., Enoki, K., Okawa, T., Nanoparticle layer detachment and its influence on the heat transfer characteristics in saturated pool boiling of nanofluids, International Journal of Heat and Mass Transfer, Vol.125 (2018), pp.171-178.

Woodfield, P.L., Monde, M., Mitsutake, Y., Implementation of an analytical two-dimensional inverse heat conduction technique to practical problems, International Journal of Heat and Mass Transfer, Vol.49, No.1-2 (2006a), pp.187-197.

Woodfield, P.L., Monde, M., Mitsutake, Y., Improved analytical solution for inverse heat conduction problems on thermally thick and semi-infinite solids, International Journal of Heat and Mass Transfer, Vol.49, No.17-18 (2006b), pp.2864-2876.

Yao, S.C., Henry, R.E., An investigation of the minimum film boiling temperature on horizontal surfaces, Transactions of American Society for Mechanical Engineers, Series C, Journal of Heat Transfer, Vol.100 (1978), pp.260-267.

Ye, Y., Cai, J., Jiang, X., Dai, D., Deng, D., Influence of groove type on welding-induced residual stress, deformation and width of sensitization region in a SUS304 steel butt welded joint, Advances in Engineering Software, Vol.86 (2015), pp.39-48.

Zhang, Y.P., Qiu, S.Z., Su, G.H., Tian, W.X., Analysis of safety margin of in-vessel retention for AP1000, Nuclear Engineering and Design, Vol.240, No.8 (2010), pp.2023-2033.

Zuber, N., On the stability of boiling heat transfer, Trans. Am. Soc. Mech. Engrs., 80 (1958).

[DOI: 10.1299/mej.20-00527]